Coupled underground blast simulation using a 2D axisymmetric Lagrangian Finite Difference Time Domain solver with a Perfectly Matched Layer

Bram Desmet[1,2], Stijn François[2], John Vantomme[1], Geert Degrande[2]

[1] Royal Military Academy, Civil and Materials Engineering Department, Renaissancelaan 30, BE-1000 Brussel, Belgium
[2] KU Leuven, Department of Civil Engineering, Kasteelpark Arenberg 40, BE-3001 Leuven, Belgium
email: {bram.desmet, john.vantomme}@rma.ac.be, {stijn.francois, geert.degrande}@bwk.kuleuven.be

ABSTRACT: Blast induced soil vibrations can cause structural damage even at large distances from the source, causing the need for accurate prediction methods. The occurrence of shock waves and the high strain rates and deformations call for the use of hydrocodes in the proximity of an explosion. At larger distance, the use of a more cost effective linear elastic calculation tool is preferred. A coupled numerical model is proposed, which combines a 2D axisymmetric Finite Difference Time Domain model in Autodyn with a frequency domain linear elastic method. The Autodyn model uses a coupled Eulerian-ALE-Lagrangian solver and is truncated in the linear elastic hydrocode domain. Spurious reflections are avoided by adding an unsplit field Perfectly Matched Layer to the truncated hydrocode domain. The results at an interface in the linear elastic hydrocode domain are used to compute results in the far field, based on the dynamic reciprocity theorem and the Green's functions of a layered elastic halfspace. The methodology is validated against a linear elastic reference solution and applied to a small subsurface explosion in a non elastic soil. The blast induced vibrations are determined at distances up to 200 m from the source and are compared to empirical reference results.

KEY WORDS: Soil wave propagation; underground blast; FDTD hydrocode; Perfectly Matched Layer; Dynamic reciprocity.

1 INTRODUCTION

Subsurface explosions cause vibrations that can have detrimental effects on structures, even at large distances. Accurate prediction of the soil vibrations is needed to control these effects.

Empirical models [1, 2] are frequently used for this purpose, but only give rough approximations based on a limited number of input parameters. Their accuracy depends on the statistical analysis of large experimental data sets.

Analytical models deliver closed form solutions to the differential equations of wave propagation, applying considerable simplifications to the geometry of the problem, the material model and the blast loading [3].

In view of these limitations, numerical modeling can provide results with more detail for realistic configurations. A hydrocode enables the simulation of highly non-linear events in the immediate surroundings of an explosion. Hydrocodes were originally developed for fluid dynamics applications, but have since been adapted to handle material strength and solid material models, enabling elasto-plastic and linear analysis. Adapted computational methodologies, combining different solver types, are used to calculate the shock wave propagation and extremely high material deformations [4]. These methods are computationally expensive and material models that cover the entire deformation range - from linear elastic to hydrodynamic - can be very complicated.

Hydrocodes have been used extensively for determining near field effects of soil blast loading. Fiserova [5] determines the effects of buried mines on protective plating with Eulerian Autodyn models, using a compaction model. Luccioni et al. [6] use a similar approach to investigate cratering by buried charges. Gu et al. [7] investigate crater formation in a layered soil using an elasto-plastic soil model in a coupled Eulerian-Aleatory Lagrangian Eulerian (ALE) setup. These models avoid the

shortcomings of the hydrocode, by limiting the extent of the modeled domain. Spurious reflections caused by this truncation do not affect the solution, since only short term and short range effects are investigated.

Hydrocode modeling of far field effects of underground blast mainly focuses on rocks, in the context of mining or underground ammunition storage. Oversized models with viscous absorbing boundary conditions (ABC) are used to reduce the effects of spurious reflections. Wu and Hao [8] study the ground motion characteristics due to a large rock chamber blast and the effects on surface structures with 2D and 3D coupled Eulerian-Lagrangian models in Autodyn. The hydrocode models extend to over 100 m from the source.

Coupled methodologies are usually limited to an Eulerian-Lagrangian coupling, where the explosive source is Eulerian and the soil is Lagrangian. Large deformations near the blast source lead to heavily distorted meshes and early termination of computations. Lu et al. [9] use a three-phase soil model [10] to determine blast induced far field effects on buried structures, using a coupled Eulerian-Smoothed Particle Hydrodynamic-Lagrangian model. The Smoothed Particle Hydrodynamics part accounts for the largest deformations surrounding the Eulerian blast source, ensuring the continued integrity of the Lagrangian part. Similarly, Jayasinghe et al. [11] use a coupled Euler-ALE model to determine the response of a foundation pile to blast induced vibration. The ALE remapping compensates for the large mesh deformations.

In this paper, a coupled numerical methodology is proposed to obtain a prediction of far field blast induced vibrations in a halfspace. Results in a bounded subdomain, surrounding the explosive source, are obtained with the Autodyn 2D axisymmetric hydrocode, using a coupled Eulerian-ALE-Lagrangian model. This subdomain is obtained by truncating the halfspace at sufficient distance from the blast source, where

the response is linear elastic. To avoid truncation errors, an 2D axisymmetric unsplit field PML for elastic media, as proposed by Kucukcoban and Kallivokas [12], is integrated in Autodyn's Lagrangian FDTD code. The tractions and displacements on an interface near the truncated edge are used to compute the elastic far field response based on the dynamic reciprocity theorem and the Green's functions of an elastic halfspace [13]. The coupled methodology is validated considering the case of a surface load on a linear elastic halfspace in section 5 and is applied on an underground explosion in a homogeneous non-linear soil. Using this methodology, blast induced vibrations in the far field can be calculated in a cost efficient manner, taking into account the non-linear behavior of the soil near the explosive source.

2 COUPLED METHODOLOGY

In the surroundings of an underground explosion, the behavior of the soil changes with growing distance from the explosive source. The 3D semi-infinite problem domain Ω is bounded by a free surface Γ_t and is divided into three subdomains Ω^1, Ω^2 and Ω^3 (figure 1). In the hydrodynamic subdomain Ω^1, immediately surrounding the explosive source S, extreme soil deformations occur at high speeds and the soil strength is exceeded: the soil behaves hydrodynamically. At a larger distance from the source, pressure waves are attenuated, but are still in the non-linear range: in the subdomain Ω^2 the soil behavior is elasto-plastic. With further attenuation of the pressure waves, the elastic limit of the soil is no longer exceeded: in the semi-infinite subdomain Ω^3, the soil has a linear elastic behavior. Subdomains Ω^1 and Ω^2 are separated by the interface Σ^{12}, while interface Σ^{23} separates subdomains Ω^2 and Ω^3.

The size and shape of subdomains Ω^1 and Ω^2 depends on the soil properties and the amplitude and depth of the blast source. For an underground explosion, the released energy is generally high enough to cause elasto-plastic soil deformations in the vicinity of the source. The stress levels are not necessarily high enough to cause hydrodynamic soil behavior. If the ratio of the depth to the amplitude of the source is sufficiently small, the subdomain interfaces Σ^{12} and Σ^{23} can intersect the free surface Γ_t. The soil at the free surface is significantly deformed, resulting in visible surface effects such as dome formation, soil ejection or cratering.

The high deformations and strain rates of the soil in the hydrodynamic domain Ω^1 require the use of computational methods and material models that can handle this non-linear behavior. The wave propagation in domain Ω^2 can be studied using non-linear, elasto-plastic methods, while in Ω^3, a linear elastic solver is used.

The complex constitutive behavior in Ω requires a computationally expensive hydrocode, applied to a bounded subdomain $\overline{\Omega}$. To avoid spurious reflections, an ABC is applied to $\overline{\Omega}$ in the linear elastic domain Ω^3. $\overline{\Omega}$ is then bounded by the truncated free surface $\overline{\Gamma}_t$ and equals $\Omega^1 \cup \Omega^2 \cup \overline{\Omega}^3$, where $\overline{\Omega}^3$ is the truncated part of Ω^3. In this work, a PML is used: Ω^{PML} is coupled to $\overline{\Omega}$ at the interface Σ^{PML} and is bounded by the free surface Γ_t^{PML} and the fixed boundary Γ_u^{PML} (figure 2).

Results in the far field, for which a hydrocode computation is not possible or cost-efficient, are obtained using a linear elastic method. The halfspace Ω^e is a linear elastic copy of
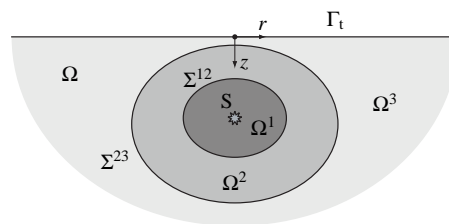

Figure 1. The problem domain $\Omega = \Omega^1 \cup \Omega^2 \cup \Omega^3$, bounded by the free surface Γ_t, containing the source S and the interfaces Σ^{12} and Σ^{23}.
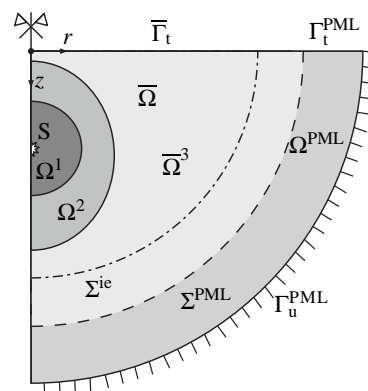

Figure 2. The truncated computational domain $\overline{\Omega} = \Omega^1 \cup \Omega^2 \cup \overline{\Omega}^3$, bounded by the truncated free surface $\overline{\Gamma}_t$, containing the source S and the interface Σ^{ie}, coupled to Ω^{PML} in Σ^{PML}.
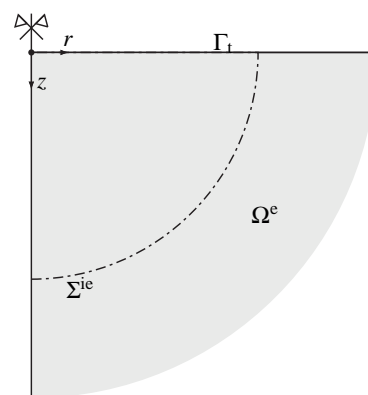

Figure 3. The linear elastic computational domain Ω^e, bounded by the free surface Γ_t, containing the interface Σ^{ie}.

Ω (figure 3). The tractions and displacements on Σ^{ie}, obtained from the calculation in $\overline{\Omega}$, are used to compute the response in Ω^e, based on the dynamic reciprocity theorem and the Green's functions of an elastic halfspace [13]. In $\overline{\Omega}$, Σ^{ie} is situated within $\overline{\Omega}^3$ (figure 2). The linear elastic material model in Ω^e matches the hydrocode material behavior in $\overline{\Omega}^3$.

3 INTERIOR SUBDOMAIN SIMULATION

The explosion source and the wave propagation in $\overline{\Omega}$ are simulated with ANSYS Autodyn, which offers a set of solvers, material models and functionalities that enable non-linear dynamic calculations [14]. The structure of the hydrocode model and the associated PML are explained.

3.1 The hydrocode model

$\overline{\Omega}$ is modeled in Autodyn, using a 2D axisymmetric Eulerian-ALE-Lagrangian multi-solver model in the time domain. This model is subdivided in coupled subgrids, each using one of these solvers. Autodyn only uses quadrilateral meshing, imposing important restrictions on the geometry and the coupling strategy of the subgrids.

The explosive source S and its gaseous explosion products are modeled using a multi-material first order Eulerian Finite Volume solver. In this part, a fine mesh is needed to obtain correct generation of the detonation wave. For small charges, this has a big impact on the time step used in the entire model. While the shape of the Euler part normally matches the explosive's shape, a spherical approximation can be adopted for compactly shaped charges. This enables a simplification of the structure of the model and has little effect on the far field results.

$\overline{\Omega}$ is modeled using a combination of Finite Difference Time Domain (FDTD) solvers: the soil near the explosive is modeled using an ALE FDTD solver. The applied motion constraints depend on the shape of the charge and the post-blast explosion cavity. The ALE part should be as small as possible, to limit the computational cost. Other ALE subgrids can be included wherever large deformations are expected. The remaining volume of the model is calculated with a Lagrangian FDTD model.

The hydrocode methodology is illustrated in detail using the application in section 6.

3.2 The Perfectly Matched Layer

Autodyn uses a 1D viscous ABC, which is supposed to absorb linear elastic waves propagating perpendicularly towards the boundary. Due to a bug in the software, only positive pressures are absorbed. To meet the truncation requirements expressed in section 2, the unsplit field 2D axisymmetric PML methodology developed by Kucukcoban and Kallivokas [12] is integrated in the Lagrangian computational cycle of Autodyn, using customizable user-subroutines.
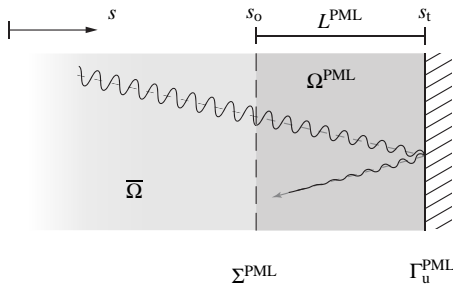

Figure 4. Ω^{PML}, coupled to $\overline{\Omega}$ in Σ^{PML}. A wave passes through Σ^{PML}, decays with distance and reflects on Γ_u^{PML}.

Consider the PML domain Ω^{PML}, coupled to $\overline{\Omega}$ at Σ^{PML}, as shown in figure 2. If s is the coordinate in the direction normal to Σ^{PML}, Ω^{PML} extends from $s = s_o$ to $s = s_t$ (figure 4). An outgoing wave passes through Σ^{PML} without reflections and decays with distance within Ω^{PML}. The coordinate s is replaced

by a stretched coordinate $\tilde{s}$, defined as [15]:

$$\tilde{s} = \int_0^s \lambda_s(s)\,\mathrm{ds} = \mathrm{s_o} + \int_{\mathrm{s_o}}^{\mathrm{s_t}} \lambda_s(s)\,\mathrm{ds} \qquad (1)$$

where $\lambda_s(s)$ is a frequency dependent, continuous, non-zero complex valued stretching function [15, 16]:

$$\lambda_s(s) = 1 + f_s^e(s) - i\frac{f_s^p(s)}{\omega}, \qquad (2)$$

where ω is the circular frequency, and the functions $f_s^e(s)$ and $f_s^p(s)$ cause attenuation of evanescent and propagating waves. Within $\overline{\Omega}$ and on Σ^{PML}, the attenuation functions are zero. This guarantees the continuity of the stretch functions across the interface and the perfectly matching properties of the PML. To obtain sufficient yet gradual attenuation within the PML, a quadratic formulation is used for $f_s^p(s)$ [12]:

$$f_s^p(s) = \begin{cases} \dfrac{3C_p}{2L^{\mathrm{PML}}}\log\left[\dfrac{1}{R}\right]\left[\dfrac{(s - s_0)}{L^{\mathrm{PML}}}\right]^2 & \text{if } s_0 \le s < s_t \\ 0 & \text{if } 0 \le s < s_0 \end{cases} \qquad (3)$$

where C_p is the dilatational wave propagation velocity and R is a reflection coefficient, indicating the needed attenuation at Γ_u^{PML}. A similar formulation is used for $f_s^e(s)$, where C_p is replaced by a characteristic length b of the domain Ω^{PML} (e.g. the cell size or L^{PML}).

In the 2D axisymmetric geometry proposed in section 3.1, the stretch is applied to the r and z coordinate. The stretch functions are introduced in the governing wave equations in the frequency domain of an axisymmetric linear elastic medium, as shown in [12]. The constitutive equation of the linear elastic medium is unaffected by the coordinate stretch. The stretched wave equations are then transformed to the time domain by an inverse Fourier transform and solved using a Lagrangian FDTD scheme, based on the Autodyn code.

A known instability issue with this type of PML is expected to cause some spurious reflections [17]. This instability can be delayed by applying a gradual, real stretch to Ω^{PML} in the direction of the stretched coordinates, without additional computational cost and with equally perfectly matching behavior of the PML. It can also be reduced by lowering the reflection coefficient R. To compensate for the reduced attenuation, Γ_u^{PML} can be replaced by a viscous ABC [18], which absorbs a large part of the remaining outgoing waves.

4 EXTERIOR SUBDOMAIN SIMULATION

The tractions $\mathbf{\bar{t}^n}$ and displacements $\mathbf{\bar{u}}$ at Σ^{ie} that result from the calculation in $\overline{\Omega}$ are imposed on Ω^{e}. The displacements in Ω^{e} can then be related to the imposed tractions and displacements by applying the dynamic reciprocity theorem [19, 20]. If body forces are neglected and Ω^{e} is initially at rest, the introduction of the Green's functions of an elastic halfspace [13] in the dynamic reciprocity equation yields the following integral representation:

$$u_i(\mathbf{x}', t) =$$
$$\int_{\Sigma^{\mathrm{ie}}} \left[u_{ij}^G(\mathbf{x}', \mathbf{x}, t) t_j^{\mathbf{n}}(\mathbf{x}, t) - t_{ij}^{G\mathbf{n}}(\mathbf{x}', \mathbf{x}, t) u_j(\mathbf{x}, t) \right] dS \qquad (4)$$

where $u_i(\mathbf{x}',t)$ is the i-th displacement component in any point $\mathbf{x}'$ in Ω^e, $u_{ij}^G(\mathbf{x}',\mathbf{x},t)$ and $t_{ij}^{Gn}(\mathbf{x}',\mathbf{x},t)$ are the Green's displacements and tractions of Ω^e and $u_j(\mathbf{x},t)$ and $t_j^{\mathbf{n}}(\mathbf{x},t)$ are the j-th component of the displacements and tractions in any point $\mathbf{x}$ on Σ^{ie}, with outward normal vector $\mathbf{n}$. A Boundary Element (BE) discretization of the integral equation at Σ^{ie}, followed by a forward Fourier transformation, allows the calculation of the wave propagation in Ω^e:

$$\hat{\underline{\mathbf{u}}}(\omega) = \hat{\mathbf{U}}(\omega)\hat{\underline{\mathbf{t}}}(\omega) - \hat{\mathbf{T}}(\omega)\hat{\underline{\mathbf{u}}}(\omega) \tag{5}$$

where an underlined variable collects vectors at multiple receivers or nodes. $\hat{\underline{\mathbf{u}}}(\omega)$ contains the displacement components at the receiver locations in Ω^e, $\hat{\underline{\mathbf{u}}}$ and $\hat{\underline{\mathbf{t}}}$ contain the components of the displacement and traction vectors applied on the interpolation nodes of Σ^{ie}. $\hat{\mathbf{U}}(\omega)$ and $\hat{\mathbf{T}}(\omega)$ are the displacement and traction BE system matrices.

5 VALIDATION

The coupled methodology is validated using the case of a concentrated surface load on a homogeneous linear elastic halfspace. In that case, $\Omega = \Omega^3$.

The material has a density $\rho = 1800$ kg/m^3, a dilatational wave velocity $C_p = 300$ m/s and a shear wave velocity $C_s = 150$ m/s. The linear elastic material model in the FDTD computation in $\overline{\Omega} \cup \Omega^{PML}$ has no hysteretic material damping. In order to validate the functioning of the coupled methodology, the material behavior in $\overline{\Omega}$ be Ω^e should correspond as much as possible. Therefore, the hysteretic material damping ratios in Ω^e, necessary for the computation of the Green's functions, are set to a very small value: $D_p = D_s = 10^{-4}$.

A vertical transient point load $F(t)$ is applied on $\overline{\Gamma}_t$ at $r = 0$, corresponding to a second order Ricker wavelet, with a characteristic frequency $f_c = 300$ Hz and an offset $t_s = 0.01$ s:

$$F(t) = \left[2\left[\pi(t - t_s)f_c\right]^2 - 1\right] e^{-[\pi(t-t_s)f_c]^2} \tag{6}$$

The geometry of the model corresponds to figures 2 and 3, where Σ^{ie}, Σ^{PML} and Γ_u^{PML} have a square shape, with sides of 2 m, 2.25 m and 3.5 m side lengths.

The displacements and tractions on Σ^{ie} are determined using the methodology presented in section 3. A Lagrangian solver is used throughout the FDTD domain. $\overline{\Omega}$ is discretized by 270 x 270 equal elements. Ω^{PML} is discretized with 30 elements in the direction normal to Σ^{PML}. This corresponds to a real stretch of 500%. The PML stretch functions $f_r^p(r)$ and $f_z^p(z)$ are quadratic and $f_r^p(2) = f_z^p(2) = 720$ Hz, which results in a reflection coefficient $R = 10^{-2}$ [12]. $f_r^e(r)$ and $f_z^e(z)$ are equal to 0: no additional real stretch is applied. The time history at Σ^{ie} is padded with zeros to a period of 1 s, to obtain an acceptable frequency resolution. A time domain window based on a sigmoid function is imposed to avoid a discontinuity between the calculated and the padded part of the time history.

The displacements in Ω^e are determined using the methodology presented in section 4. Σ^{ie} is discretized with 240 equally sized, nodally collocated BEs, that coincide with the hydrocode element faces at Σ^{ie}. The Green's functions of an elastic halfspace are used to obtain reference solutions in Ω^e and on Σ^{ie}, using EDT [13].
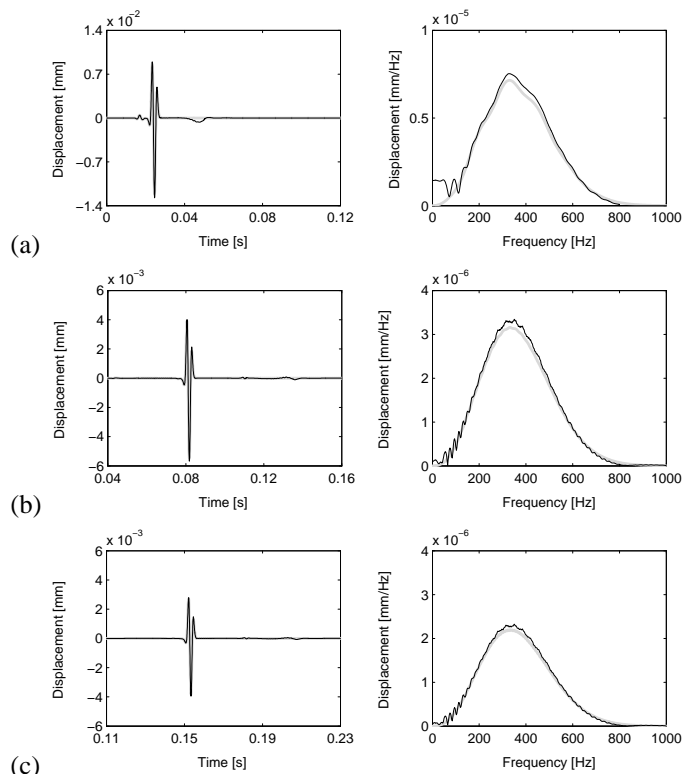

(a)

(b)

(c)

Figure 5. Time history (left) and frequency content (right) of the vertical displacement at (a) $(r,z) = (2,0)$ m, on Σ^{ie}, (b) $(r,z) = (10,0)$ m and (c) $(r,z) = (20,0)$ m. The reference solution (black) is compared to the coupled solution (gray).

Figure 5(a) compares the vertical displacement on Σ^{ie} at $(r,z) = (2,0)$ m of the FDTD simulation to the reference solution. The small amplitude difference is the result of the absence of hysteretic material damping in the FDTD material model. Small spurious vibrations due to the onset of the PML instability appear between 0.04 and 0.05 s. They appear more clearly in the frequency domain, where the low frequency range of the FDTD solution deviates from the reference solution.

Figures 5(b) and 5(c) compare the results of the coupled calculation to the reference solution in Ω^e at $(r,z) = (10,0)$ m and $(r,z) = (20,0)$ m. The small amplitude difference between both solutions, as observed in figure 5(a), does not change at larger distances from the source, since the material damping in Ω^e of the coupled solution and in the reference solution is identical. Apart from this amplitude offset, the results are satisfactory and prove the validity of the coupled methodology.

Since the PML induced instability is situated in the low frequency range, it is attenuated less than the high frequency content of the outgoing wave; its influence is therefore expected to become more prominent at larger distance from Σ^{ie}. In this validation, this is prevented by the very low attenuation coefficient. When considering materials with a higher material damping ratio, the PML induced error can dominate the solution at large distances from the source. A more stable PML formulation for Autodyn or the application of an improved time domain window or high-pass frequency filter on the results at Σ^{ie} can solve this problem.

6 APPLICATION

The coupled methodology is applied to the underground explosion of a 1 kg sphere of C4 explosive at a depth of 2 m in a homogeneous halfspace.

A single soil model is used throughout $\overline{\Omega}$, based on the model of Luccioni et al. [6]. The bulk compressibility of the soil is modeled using a Mie-Grüneisen equation of state, based on the shock Hugoniot of the material [14]. The hydrodynamic pressure $p(t)$ equals

$$p(t) = p_H(t) + \gamma \rho_0 \left[e(t) - \frac{p_H(t)\mu(t)}{2\rho_0(1+\mu(t))} \right] \quad (7)$$

where the Hugoniot pressure $p_H(t)$ is

$$p_H(t) = \frac{\rho_0 \, \mu(t)\,(1+\mu(t))\, \sqrt{C_p{}^2 - \frac{4}{3}C_s{}^2}}{[1-(s_H-1)\mu(t)]^2} \quad (8)$$

with $\gamma = 0.11$ the Grüneisen coefficient, $s_H = 1.5$ the linear shock Hugoniot slope coefficient, $\rho_0 = 1920$ kg/m³ the soil density, $C_p = 600$ m/s the dilatational wave velocity, $C_s = 300$ m/s the shear wave velocity, $\rho(t)$ the density, $e(t)$ the specific internal energy and $\mu(t) = [\rho(t)/\rho_0] - 1$ the compression rate. ρ_0, C_p and C_s are considered at $p = 0$. A hydrodynamic bulk failure limit pressure p_{min} is set at -1 MPa. In terms of Von Mises stress, the yield strength σ_y is determined by a piecewise linear Drucker-Prager criterion:

$$\sigma_y = \begin{cases} \alpha p + \beta \,[\text{MPa}] & \text{if } p_{min} \le p \le 6.88\,\text{MPa} \\ 6.2\,\text{MPa} & \text{if } \quad\quad p > 6.88\,\text{MPa} \end{cases} \quad (9)$$

where $\alpha = 0.74$ and $\beta = 1.11$ MPa depend on the soil's cohesion and internal friction angle. At low pressures, this material model approaches a linear elastic model, with wave velocities C_p and C_s and density ρ_0. This model is used in Ω^{PML}. In Ω^e, this material is used in combination with hysteretic material damping ratios $D_p = D_s = 0.02$. The explosive material model is the Jones-Wilkins-Lee equation of state for C4, as used in Autodyn [6, 14].

In this case, it is possible to perform the hydrocode simulation in two steps. The first 2.55 milliseconds after the detonation are modeled with an Eulerian 1D spherical symmetric starter model. It has a length of 2 m from the center of the explosive to the free surface and is discretized by 2000 equally sized elements. The explosive, which has a radius of 0.055 m, is situated at the center of this model and is surrounded by soil. The wave propagation is modeled from the detonation up to the moment the shock wave reaches the free surface. The 1D results are subsequently remapped onto the full model, which has been dimensioned to correspond to the deformed state at the end of the 1D simulation. The radius of the explosive products R_1 at $t = 2.55$ ms equals 0.268 m.

The starter model contains explosive and soil material in a single multi-material Eulerian mesh. The interface between both materials risks blurring due to diffusion [21]. If soil material is remapped into the Euler part of the full model, this leads to local errors in the Eulerian part and in the fluid-structure interface and can stop or delay the computation.

The use of a two step hydrocode methodology has several advantages. Autodyn uses explicit time integration with a
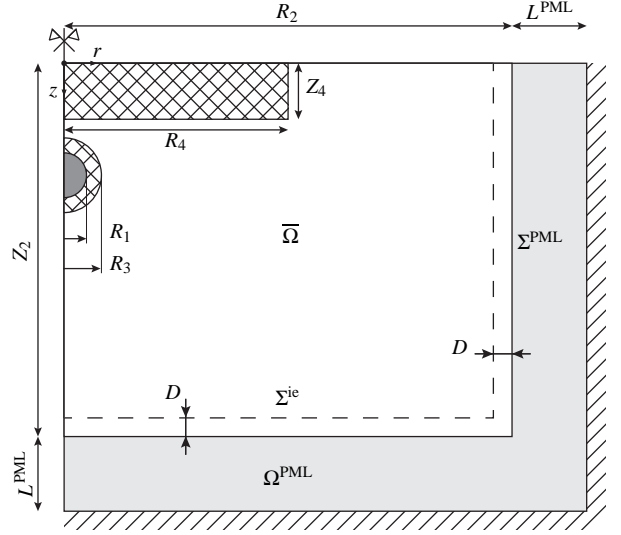

Figure 6. Hydrocode domain $\overline{\Omega}$ and Ω^{PML}, indicating the Eulerian (dark) and ALE (double hatched) calculation domains.

leapfrog second order time integrator. The time step, which is identical for all subgrids in the model, is determined at each time step, based on the Courant-Friedrichs-Lewy stability condition. It depends on the cell size and the local dilatational wave propagation velocity. The very high velocities and dense mesh needed for the high quality simulation of the initial shock wave generation near the explosive source result in extremely small time steps. In the two step methodology, this is limited to the 1D starter model. By the end of the its computation, the velocities in the soil have dropped and a dense mesh near the source is no longer needed. This allows for larger time steps and coarser meshes for the full model computation.

In the second step, the results of the starter model are propagated in the full model, which contains the hydrocode calculation domain $\overline{\Omega}$ and the PML (figure 6). The size of $\overline{\Omega}$ is $R_2 = 6$ m by $Z_2 = 5$ m and it is modeled using a combination of Finite Difference Time Domain (FDTD) solvers on different coupled subgrids. The preferred size of these subgrids is determined by running preliminary simulations with a coarse mesh.

The Eulerian calculation domain is limited to the spherical volume of the explosive source at $t = 2.55$ ms, with a radius R_1 and is meshed with equally sized, 10 mm by 10mm cells.

The Eulerian domain is surrounded by an ALE domain with radius $R_3 = 0.5$ m and a radial expansion ALE constraint on a radial mesh. This configuration is most practical for matching the expanding explosion cavity and preserving the shape of the outgoing wave near a compact charge [21]. A second, rectangular ALE domain is situated at the free surface to handle the large deformations caused by the reflected pressure wave. The size of this domain is $R_4 = 2$ m by $Z_4 = 0.6$ m. A bilinear ALE constraint is applied, according to the axes of the nodal coordinate system of the model. Since the time steps are small, the cell deformation per time step is limited and satisfactory results can be obtained when performing the ALE remapping every 5 to 10 time steps, reducing the cost of the

ALE remapping. Nodes at subgrid interfaces are not subjected to the ALE motion constraints, to ensure correct coupling.

The remaining parts of $\overline{\Omega}$ use the Lagrangian FDTD solver and are meshed with equally sized, 10 mm by 10 mm cells. At large distances from the blast source, spherical meshing needs to be avoided, since acceptable cell size ratios can only be obtained by introducing multiple transition parts, which needlessly complicate the structure of the model. In this configuration, only one transitional discretization subgrid is needed to couple the rectangular Lagrangian subgrid to the radial ALE subgrid.

Ω^{PML} uses the adapted Lagrangian FDTD solver discussed in section 3.2. The domain has a width $L^{\mathrm{PML}} = 1$ m and is discretized with 50 rectangular elements in the direction normal to Σ^{PML}, with a linearly increasing real stretch. The PML stretch functions $f_r^p(r)$ and $f_z^p(z)$ are quadratic and $f_r^p(7) = f_z^p(6) = 1800$ Hz, which results in a reflection coefficient $R = 10^{-2}$ in accordance with the stretch formulations in [12]. $f_r^e(r)$ and $f_z^e(z)$ are constant and equal to 1: no additional real stretch is applied.

Σ^{ie} is parallel to the Σ^{PML} interface, at a distance of $D = 0.15$ m. This interface is discretized with 1070 equally sized and nodally collocated BEs that coincide with the hydrocode element faces at Σ^{ie}.

The average time step of the hydrocode simulation is 5×10^{-3} ms, for a duration of 50 ms. Figure 7 shows the norm of the velocity field in $\overline{\Omega}$ at different time steps. At 2.55 ms, immediately after the exportation of the starter model data to the full model (figure 7(a)), the spherically symmetric pressure wave approaches the free surface. High velocities surrounding the explosion cavity indicate its ongoing expansion.

At 4 ms (figure 7(b)), the dilatational blast wave has hit and reflected from the free surface surrounding the epicenter. High particle velocities occur where the soil has failed: the tensile stresses from the reflected dilatational wave have reached $p_{\min}$. In reality, this would result in a projection of soil particles. In this model, this large deformation is handled by the ALE solver. For extended simulations, it can lead to excessive mesh deformation. Extended time histories can be computed by applying an erosion rule or by the local use of a particle method.

At 8 ms (figure 7(c)), this expansion has nearly stopped. The dilatational wave is transmitted without reflection into Ω^{PML}. A reflected dilatational and shear wave follow the main dilatational wave. The noise behind the leading dilatational wave results from the slow expansion and pulsation of the explosion cavity and the interaction of reflected waves with this cavity.

At 11 and 20 ms (figures 7(d) and 7(e)), the explosion cavity has stabilized completely. The leading dilatational wave and the reflected waves as well as the trailing vibrations are correctly transmitted. A distinct surface wave has not developed within $\overline{\Omega}$.

At 50 ms (figure 7(f)), $\overline{\Omega}$ is silent, except for the spalling action at the free surface near the epicenter. There is some indication of the instability of the PML affecting $\overline{\Omega}$ near the right edge of the domain.

Figure 8 shows the non-elastic domain $\Omega^1 \cup \Omega^2$ within $\overline{\Omega}$ that has undergone plastic deformation and/or tensile failure. The extension of this domain along the free surface is caused by the reflection of the dilatational blast wave. This reflected wave induces tensile stress and therefore lower yield strength in
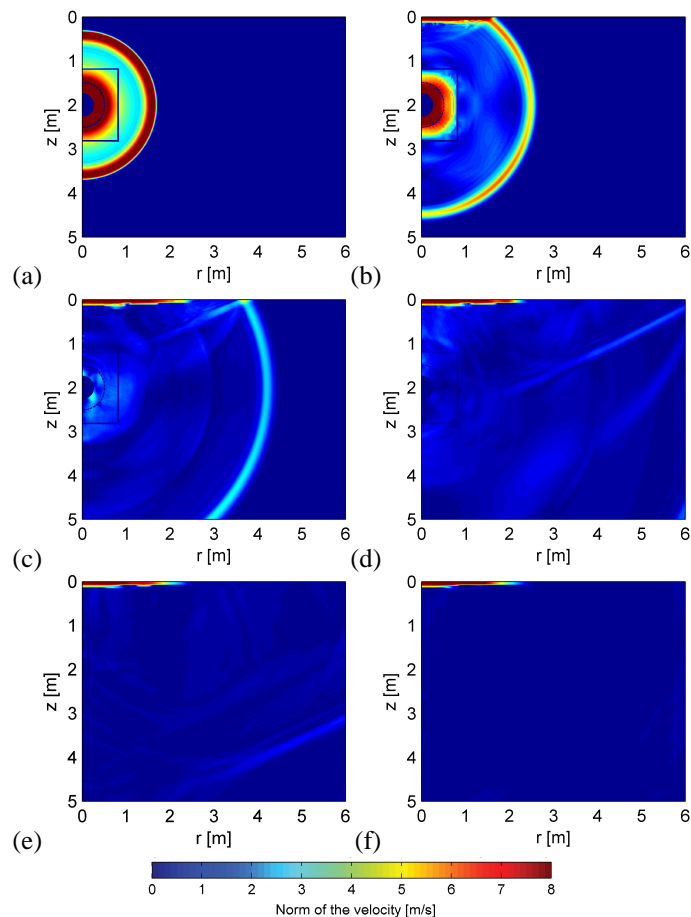

Figure 7. Norm of the velocity field in $\overline{\Omega}$ at (a) 2.55 ms, (b) 4 ms, (c) 8 ms, (d) 11 ms, (e) 20 ms and (f) 50 ms.
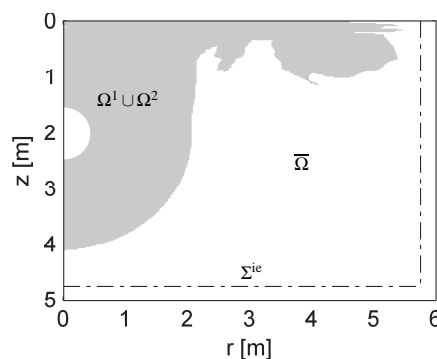

Figure 8. The non-elastic domain $\Omega^1 \cup \Omega^2$ (gray) in $\overline{\Omega}$ and Σ^{ie}.

the top layer of the soil. The shape of the plastic deformation domain justifies the use of a rectangularly shaped $\overline{\Omega}$ and Σ^{ie}.

Figure 9 shows the components of the velocities and tractions, normal and tangential to the interface Σ^{ie} at the free surface. The high frequency content of the waveforms is explained by the lack of material damping and the time history of the explosive source, which approximates an impulse. This justifies the use of a dense mesh throughout $\overline{\Omega}$. The outgoing waves are transmitted properly into Ω^{PML} but the velocities and tractions do not attenuate entirely before the onset of the PML instability.
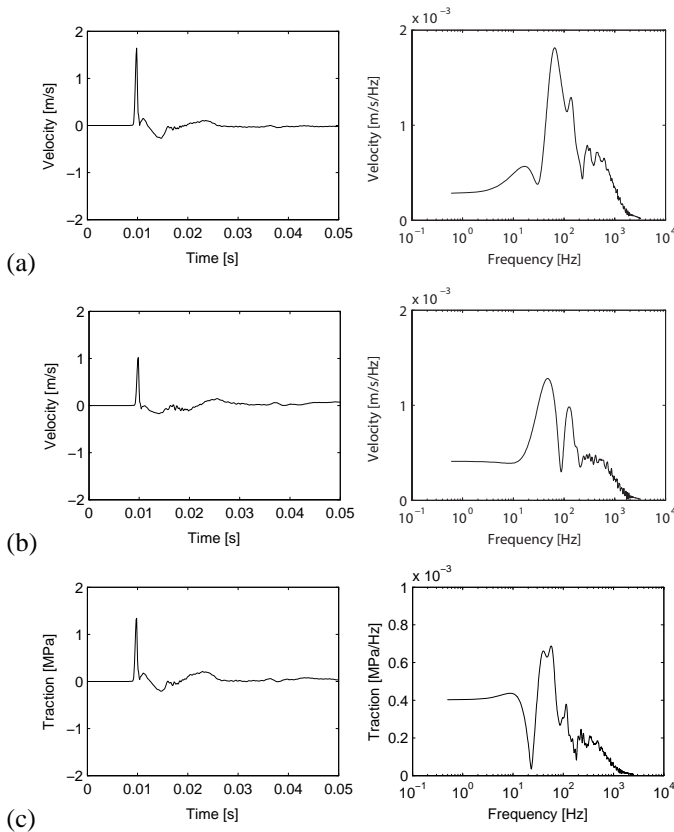
Figure 9. Time history (left) and frequency content (right) of the (a) normal and (b) and tangential component of the velocity and (c) the normal component of the tractions on Σ^{ie} at $z = 0$.

The time histories of the velocities and tractions on Σ^{ie} are padded with zeros to a period of 2 s. A time domain window based on a sigmoid equation is applied to smoothen the transition between the the original time histories and the padded extensions. The application of this window enhances the quality of future frequency domain transformations and, in addition, reduces the effect of the instability of the PML. The displacements at Σ^{ie} are obtained from the padded time histories of the velocities. To avoid discontinuities, a similar time domain window is applied to attenuate the final 5 ms of the padded displacement time histories. The velocities and tractions are then transformed to the frequency domain, using a forward Fourier transform.

The displacements in Ω^{e} are obtained in the frequency domain according to the procedure presented in section 4 and are derived to obtain the velocities. These are transformed to the time domain using an inverse fast Fourier transform. Figures 10 and 11 show the velocities at the free surface, at 10 and 50 m from the epicenter of the explosion. The leading dilatational wave dominates the wave form for tens of meters from the epicenter. A surface wave has developed, but its amplitude is of the same order of magnitude as the dilatational wave. Due to the high frequency content of the input, the frequency content of the waves is high, even at large distances from the source.

The effects of the instability of the PML, as seen in section 5, are not observed in this application. This can be attributed to the
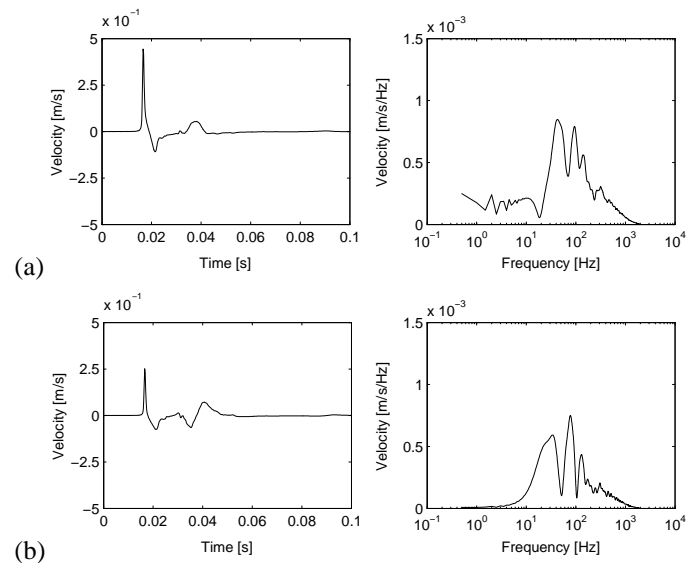

Figure 10. Time history (left) and frequency content (right) of the radial (a) and vertical component (b) of the velocity at 10 m from the epicenter.
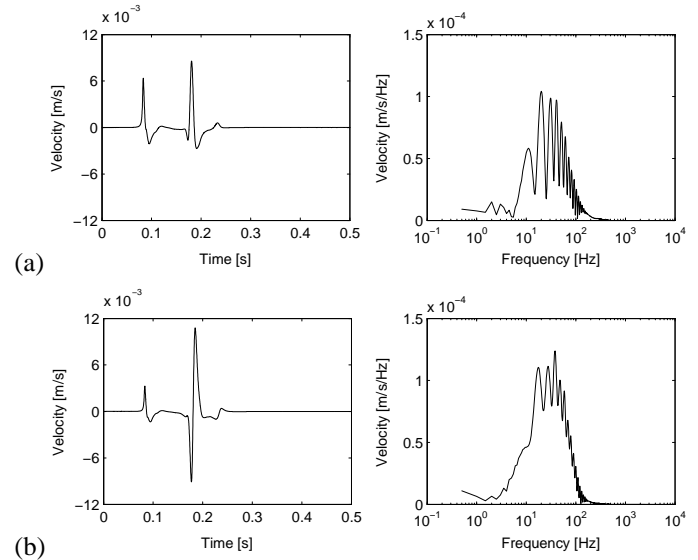

Figure 11. Time history (left) and frequency content (right) of the radial (a) and vertical component (b) of the velocity at 50 m from the epicenter.

high frequency content of the input, which reduces the relative importance of the low frequency instabilities.

The peak particle velocity (PPV) is determined for the radial and vertical velocity component at a series of points at the free surface in $\overline{\Omega}$ and Ω^{e}, from 3 to 200 m from the epicenter of the explosion. This distance is scaled by the cube root of the TNT equivalent weight of the C4 explosive, which is 1.32 kg. The computed PPVs are compared to empirical reference relationships. The empirical formulation for the PPV developed by Drake and Little [2] is valid up to a scaled distance of 5 m/$\sqrt[3]{\mathrm{kg}}$. This formulation only depends on the soil properties through an attenuation coefficient m. It is used as a reference in $\overline{\Omega}$ with attenuation coefficients $m = 2.25$ and $m = 1.5$. The first value is estimated based on ρ_0 [2], while the second value corresponds to a soil with low material damping [22]. Westine's relationships for the radial PPV [1] is
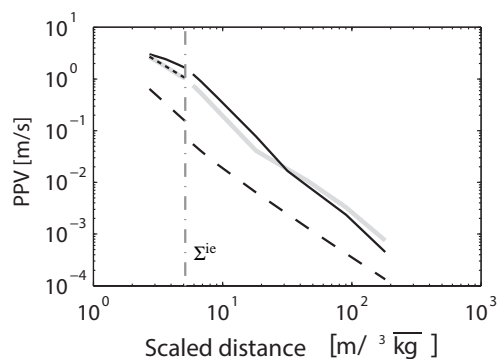
Figure 12. PPV in function of scaled distance. Radial (black) and vertical (gray) components are compared to empirical reference results with regular (dashed) and with very low material damping (dotted).

valid up to 245 m/$\sqrt[3]{kg}$ and is used in Ω^e. This relationship is a function of the density ρ_0 and the dilatational wave velocity C_p of the soil.

The computed PPVs are consistently higher than the empirical relationships of Westine [1] and Drake and Little [2] with $m = 2.25$ (figure 12). The attenuation of the computed radial PPVs in the linear elastic domain, which corresponds to the angle of inclination of the curves, corresponds well to Westine's reference result, but depends strongly on the choice of D_p and D_s. The formulation of Drake and Little with $m = 1.5$ (dotted line in figure 12(a)) has a very good correspondence with the computed FDTD results in $\overline{\Omega}$. This improved correspondence can be attributed to the absence of material damping in the hydrocode soil model. This results in a strong similarity with the parameters for a soil with low damping, as used in the empirical approach where $m = 1.5$.

Only limited conclusions can be drawn from this comparison, since only one computed result is compared to empirical methods for which the statistical parameters are unknown. It does however indicate the large impact of the material damping in the relatively small hydrocode domain on the results of the coupled method at large distances.

7 CONCLUSIONS

In this paper, a coupled methodology is presented to calculate the wave propagation due to an underground explosion, to overcome the limitations imposed by analytical and empirical modeling. The method successfully combines an Autodyn hydrocode computation for the soil near the blast source with a cost efficient linear elastic model, based on the dynamic reciprocity theorem and the Green's functions of an elastic halfspace. Within the bounded hydrocode domain, different solvers - Eulerian, ALE and Lagrangian - are combined to obtain a coherent solution to the non-linear blast induced wave propagation. A PML is integrated in the Autodyn code to avoid spurious reflections on the truncated edges of the hydrocode domain.

The accuracy of the methodology is demonstrated in a linear elastic validation example. The low frequency PML induced instability errors, which seem negligible at first, are shown to gain importance with increased attenuation of the outgoing wave. Increased accuracy can be obtained by improving the

stability of the PML implementation or by reducing the impact of the PML induced instability.

The method is successfully applied to an underground explosion in a halfspace, using a non-linear soil model in the hydrocode calculation domain. The application indicates the possibility to determine blast induced vibrations at large distances from the source. A comparison to empirical reference methods shows that the velocities obtained by this specific application of the coupled methodology are considerably higher and that the absence of material damping in the hydrocode soil model has a large impact on the results of the coupled methodology.

ACKNOWLEDGEMENTS

REFERENCES

[1] P.S. Westine. Ground shock from the detonation of buried explosives. *Journal of Terramechnics*, 15(2):69–79, 1978.
[2] J.L. Drake and C.D. Little. Ground shock from penetrating conventional weapons. In *Proceedings of the 1st Symposium on The Interaction of Non-nuclear munitions with Structures*, Colorado, May 1983.
[3] J.A. Sharpe. The production of elastic waves by explosion pressures. I. Theory and empirical field observations. *Geophysics*, 7(3):144–154, 1942.
[4] J.A. Zukas. *Introduction to hydrocodes*. Elsevier, 2004.
[5] D. Fiserova. *Numerical analysis of buried mine explosions with emphasis on effect of soil properties on loading*. PhD thesis, Cranfield, 2006.
[6] B. Luccioni, D. Ambrosini, G. Nurick, and I. Snyman. Craters produced by underground explosions. *Computers & Structures*, 87(21-22):1366 – 1373, 2009.
[7] Q. Gu, F. H. Lee, and K.H. Chee. Numerical simulation of explosive-induced cratering. In *Proceedings of the 11th International Symposium on Interaction of the Effects of Munition with Structures (ISIEMS 11)*, Mannheim, Germany, May 2003.
[8] C. Wu and H. Hao. Numerical study of characteristics of underground blast induced surface ground motion and their effect on above-ground structures, Part 1: Ground motion characteristics. *Soil Dynamics and Earthquake Engineering*, 25:27–38, 2005.
[9] Y. Lu, Z. Wang, and K. Chong. A comparative study of buried structure in soil subjected to blast loading using 2D an 3D numerical simulations. *Soil Dynamics and Earthquake Engineering*, 25:275–288, 2005.
[10] Z. Wang, H. Hao, and Y. Lu. A three-phase soil model for simulating stress wave propagation due to blast loading. *International Journal for Numerical and Analytical Methods in Geomechanics*, 28:33–56, 2004.
[11] L.B. Jayasinghe, D.P. Thambiratnam, N. Perera, and Jayasooriya J.H.A.R. Computer simulation of underground blast response of pile in saturated soil. *Computers & Structures*, 120:86 – 95, 2013.
[12] S. Kucukcoban and L.F. Kallivokas. A mixed perfectly-matched-layer for transient wave simulations in axisymmetric elastic media. *Computer Modeling in Engineering and Sciences*, 64(2):109–145, 2010.
[13] M. Schevenels, S. François, and G. Degrande. EDT: An ElastoDynamics Toolbox for MATLAB. *Computers & Geosciences*, 35(8):1752–1754, 2009.
[14] ANSYS Inc. *Autodyn, Explicit Software for Non-linear Dynamics, Theory Manual*, revision 4.3 edition, 2005.
[15] W.C. Chew and Q.H. Liu. Perfectly matched layers for elastodynamics: A new absorbing boundary condition. *Journal of Computational Acoustics*, 4(4):341–359, 1996.
[16] J.P. Bérenger. A perfectly matched layer for the absorption of electromagnetic waves. *Journal of Computational Physics*, 41:115–135, 1994.
[17] J.F. Semblat and A. Pecker. *Waves and vibrations in soils: earthquakes, traffic, shocks, construction works*. IUSS Press, 2009.
[18] Z. Jiang, J.C. Bancroft, and L.R. Lines. Combining absorbing and nonreflecting boundary conditions for elastic wave simulation. *CREWES Research Report*, 21, 2009.
[19] A.C. Eringen and E.S. Suhubi. *Elastodynamics, Volume 2, Linear theory*. Academic Press, New York, USA, 1975.
[20] L.T. Wheeler and E. Sternberg. Some theorems in classical elastodynamics. *Archive for Rational Mechanics and Analysis*, 31:51–90, 1968.
[21] B. Desmet, J. Vantomme, and G. Degrande. Numerical prediction of blast induced wave propagation in the soil. In *Proceedings of COMPDYN 2009, 2nd International Conference on Computational Methods in Structural Dynamics and Earthquake Engineering*, Rhodes, Greece, June 2009. CD-ROM.
[22] C.H. Dowding. *Construction vibrations*. Prentice Hall, 1996.